

CORNELL UNIVERSITY LIBRARY

Subscriber access provided by CORNELL UNIVERSITY LIBRARY

Article

Colocalized Nanoscale Electrical and Compositional Mapping of Organic Solar Cells

Jeremy S. Mehta, Pravini S. Fernando, John L. Grazul, and Jeffrey M. Mativetsky

ACS Appl. Energy Mater., Just Accepted Manuscript • DOI: 10.1021/acsaem.9b00829 • Publication Date (Web): 20 Jun 2019

Downloaded from http://pubs.acs.org on June 25, 2019

Just Accepted

"Just Accepted" manuscripts have been peer-reviewed and accepted for publication. They are posted online prior to technical editing, formatting for publication and author proofing. The American Chemical Society provides "Just Accepted" as a service to the research community to expedite the dissemination of scientific material as soon as possible after acceptance. "Just Accepted" manuscripts appear in full in PDF format accompanied by an HTML abstract. "Just Accepted" manuscripts have been fully peer reviewed, but should not be considered the official version of record. They are citable by the Digital Object Identifier (DOI®). "Just Accepted" is an optional service offered to authors. Therefore, the "Just Accepted" Web site may not include all articles that will be published in the journal. After a manuscript is technically edited and formatted, it will be removed from the "Just Accepted" Web site and published as an ASAP article. Note that technical editing may introduce minor changes to the manuscript text and/or graphics which could affect content, and all legal disclaimers and ethical guidelines that apply to the journal pertain. ACS cannot be held responsible for errors or consequences arising from the use of information contained in these "Just Accepted" manuscripts.

Colocalized Nanoscale Electrical and Compositional Mapping of Organic Solar Cells

Jeremy S. Mehta,¹ Pravini S. Fernando,¹ John L. Grazul,² Jeffrey M. Mativetsky^{1*}

¹Department of Physics, Applied Physics, and Astronomy, Binghamton University, Binghamton, NY 13902, USA

²Cornell Center for Materials Research, Cornell University, Ithaca, NY 14853, USA

*E-mail: jmativet@binghamton.edu

ABSTRACT

Organic photovoltaics based on the bulk heterojunction is an emergent technology with the potential to enable low-cost, lightweight, and mechanically flexible energy conversion applications. Organic photovoltaic performance is intimately linked to the heterogeneous nanoscale structuring of the active layer. Means of directly assessing the interplay between local nanoscale structure and local nanoscale function is lacking, however. This work combines the complementary strengths of energy-filtered transmission electron microscopy and conductive atomic force microscopy to perform colocalized nanoscale measurements of bulk heterojunction chemical composition and charge carrier mobility in a high-performance small molecule organic photovoltaic system. We find that nanoscale donor concentration and hole mobility maps are uncorrelated, unlike device-scale measurements that show a strong dependence of hole mobility on donor concentration. These results challenge standard interpretations of nanoscale structural and electrical maps, e.g., that a high local donor concentration implies a high local hole mobility and vice versa. Our results demonstrate instead that factors such as local phase continuity have a greater impact on charge transport than the local amount of each phase. These results also support an emerging picture for small molecule bulk heterojunctions in which electrical connectivity within finely mixed domains plays a decisive role in charge migration. The devised colocalized approach is generalizable to a broad range of transmission electron microscope and atomic force microscope modes, opening vast opportunities for nanoscale structure-function mapping of materials.

Keywords:

organic solar cell, bulk heterojunction, charge transport, composition, conductive atomic force microscopy, transmission electron microscopy

INTRODUCTION

Organic photovoltaics (OPVs) has emerging potential to meet the growing demand for green, cost-efficient, and versatile energy conversion technologies. 1–5 Efficient OPV operation is achieved through a nanostructured bulk heterojunction (BHJ) architecture that features an interpenetrating, three-dimensional network of pure and finely mixed donor and acceptor components. The high density of donor-acceptor interfaces enables efficient exciton dissociation, while the continuity of the constituent phases allows for charge transport and collection. 6–8 The sensitive interplay between nanoscale morphology and photovoltaic function in BHJ active layers motivates the need for characterization that goes beyond ensemble-averaged properties and device-scale performance. Insight into the underlying mechanisms that govern OPV performance can be gleaned by examining the microscopic anatomy of BHJs and the functional roles played by their constituent parts.

Transmission electron microscopy (TEM) has been a valuable tool for monitoring local BHJ domain size, connectivity, crystallinity, and chemical composition. ^{9–13} By resolving molecular lattice fringes, it has been possible to track molecular orientation and stacking structure in individual domains. ^{10,13–15} Cross-sectional imaging has revealed vertical donor-acceptor phase segregation, ^{13,14} while tomography has enabled the three-dimensional visualization of nanoscale domain networks. ^{11,16,17} Moreover, energy filtered TEM (EF-TEM) has made it possible to map local chemical composition, to investigate BHJ domain morphology and purity. ^{9,11,18–20} Nevertheless, despite the importance of TEM for the nanoscale structural characterization of OPV active layers, TEM provides little insight into local optoelectronic performance.

Conductive atomic force microscopy (C-AFM) makes it possible to measure the nanoscale optoelectronic properties of OPV active layers by using a metal-coated AFM probe as a movable electrode.^{21,22} Current mapping has been used to track the formation and improvement of charge transport pathways as a function of annealing,^{23,24} and other film processing conditions.^{12,25–27} Under light illumination, C-AFM has revealed local photocurrent variations,^{28–32} allowing the observation of anticorrelated photocurrent and dark-current features, a result that highlights the contrasting morphological requirements for charge photogeneration and charge transport.³³ Recently, point-by-point current-voltage (PPIV) C-AFM mapping^{25,34,35} has been introduced to enable quantitative analysis of large arrays of local current-voltage characteristics. With this approach, charge carrier mobility,^{25,36} open circuit voltage,³⁵ and other photovoltaic properties³⁵ have been spatially mapped with nanoscale resolution. These studies have made it possible to visualize the evolution of local charge carrier mobility across a broad range of BHJ morphologies²⁵ and to identify performance bottlenecks in hybrid organic-inorganic nanorod solar cells.³⁵ An

ongoing challenge with C-AFM and PPIV mapping, however, has been in identifying the structural origin of the measured properties.

While TEM and C-AFM have highly complementary capabilities (and shortcomings), technical challenges have prevented the application of these methods for colocalized nanoscale structure-function analysis. In this work, we establish protocols for performing EF-TEM and PPIV C-AFM at the same sample location, and then investigate the interplay between nanoscale composition and local charge transport in a high-performance small molecule BHJ system.

We find, surprisingly, that local hole mobility exhibits no discernible correlation with local donor concentration. This result is in contrast with device-scale measurements that show a strong dependence of hole mobility on donor concentration. 9,10,37,38 The lack of correlation runs counter to common interpretations of nanoscale BHJ data, e.g., that a high local donor concentration implies efficient local hole transport, and vice versa. Furthermore, these results reveal the importance of finely mixed domains in mediating charge migration in small molecule BHJs. By introducing a metric that tracks the local electrical connectivity within the film, our analysis demonstrates that local molecular arrangement has a greater impact on charge transport than the local amount of each phase.

RESULTS AND DISCUSSION

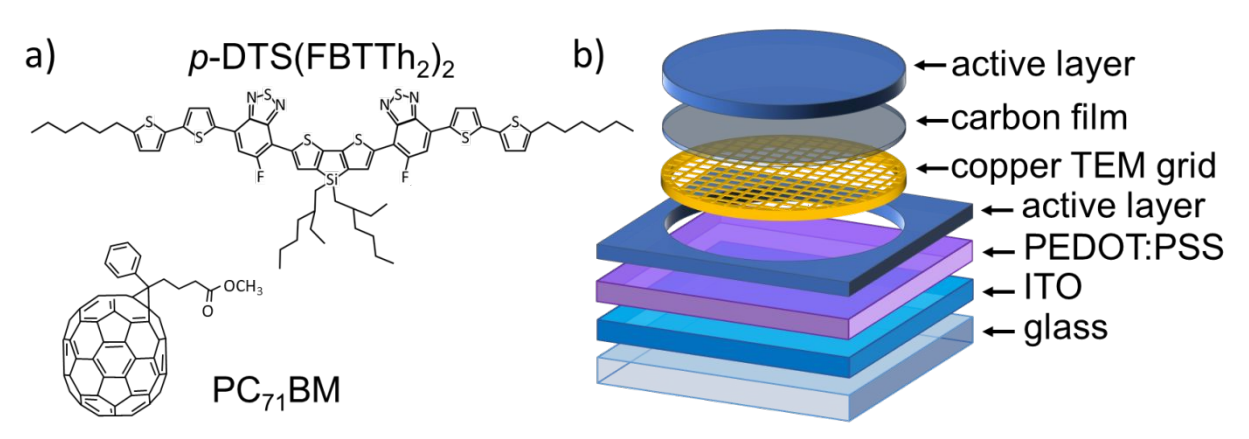


Figure 1. (a) Molecular structure of p-DTS(FBTTh₂)₂ and PC₇₁BM. (b) Exploded view of the sample structure.

BHJ thin films were prepared comprising small molecule electron donor 7,7'- (4,4-bis(2-ethylhexyl)-4H-silolo[3,2-b:4,5-b']dithiophene-2,6-diyl)bis(6-fluoro-4-(5'-hexyl-[2,2'-bithiophen]-5-yl)benzo[c][1,2,5]thiadiazole) (p-DTS(FBTTh₂)₂) and fullerene acceptor

phenyl- C_{71} -butyric acid methyl ester (PC₇₁BM) (Figure 1a). This BHJ system has exhibited a power conversion efficiency as high as 8.9%.³⁹

To enable TEM and C-AFM measurements at the same sample location, the BHJ was prepared directly on a carbon-coated TEM grid. By mounting the grid on a glass substrate coated with indium tin oxide (ITO) and poly(3,4-ethylenedioxythiophene) polystyrene sulfonate (PEDOT:PSS), it was possible to spin-coat the active layer onto the grid and the surrounding substrate (Figure 1b). This procedure bypasses the need to float the organic active layer in water for transfer to a TEM grid, 9,40,41 a process which may disrupt the properties of the film or lead to film fragmentation. Furthermore, by simultaneously depositing the active layer onto the TEM grid and a standard OPV substrate, we can verify that the film morphology and charge transport characteristics are comparable in both cases. As shown in Supporting Information Figure S1, both films exhibit a highly similar topography, with similar C-AFM current features, and an average current level that differs by less than 3%. It should be noted that the C-AFM measurements on the grid were performed while the grid was electrically contacted to the PEDOT:PSS/ITO/glass substrate using silver paint. The grid was separated from the underlying substrate for subsequent TEM characterization. The use of a TEM grid for both the C-AFM and TEM measurements also facilitates the process of finding the same sample location, by employing the grid lines for spatial indexing.

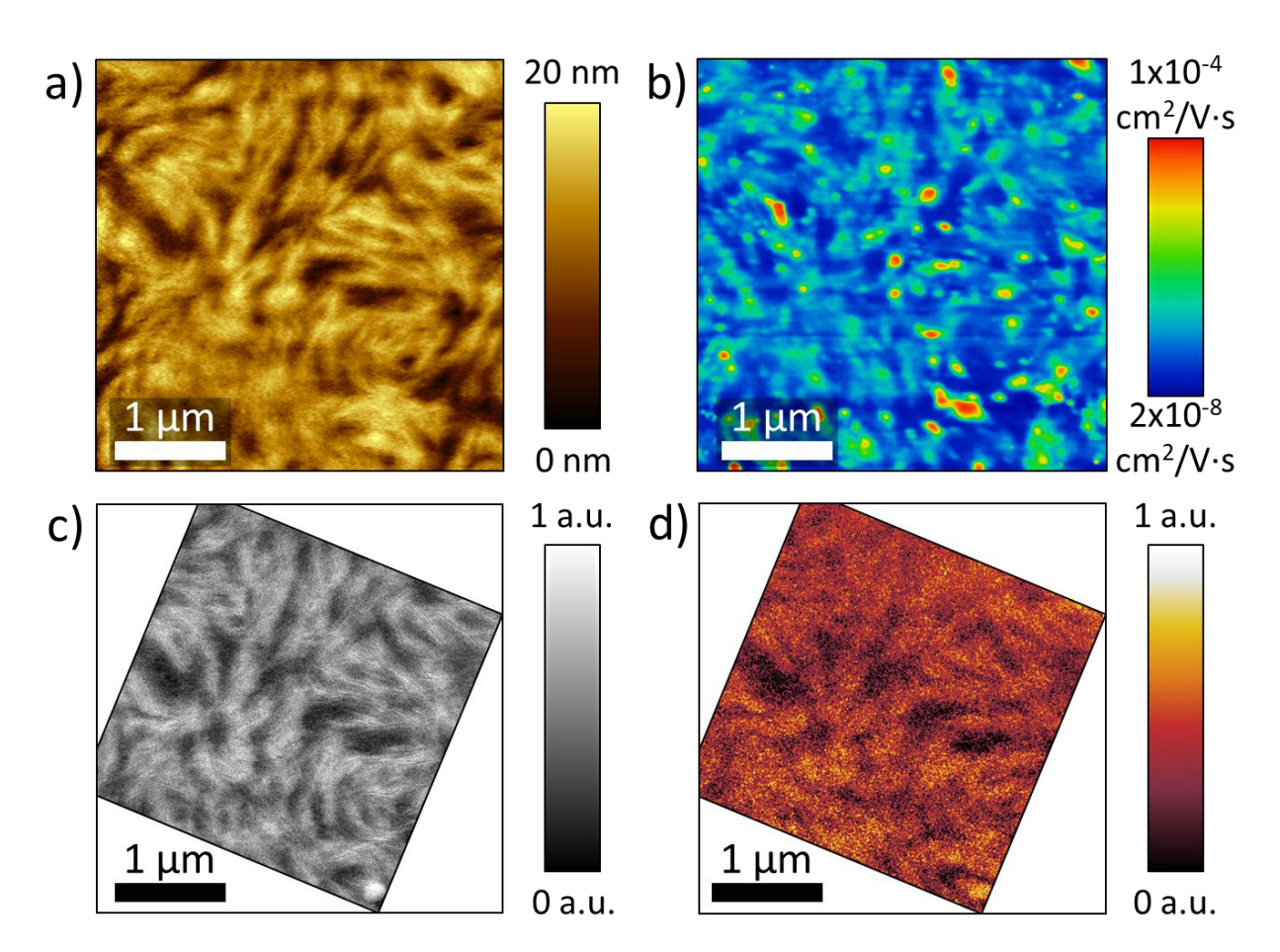


Figure 2. Structural and electrical mapping at the same location of a p-DTS(FBTTh₂)₂:PC₇₁BM film: (a) topography acquired during PPIV mapping, (b) PPIV hole mobility, (c) thickness measured by TEM, and (d) donor concentration.

Topography and hole mobility (Figure 2a and 2b) were spatially mapped using PPIV C-AFM.^{25,34,35} Briefly, height and current-voltage characteristics were recorded at 134,000 sample positions and a modified space-charge limited current model was used to extract hole mobility at each sample location, with a 10 nm pixel resolution. The topography exhibits that (Figure 2a) fiber-like structures are characteristic of p-DTS(FBTTh₂)₂:PC₇₁BM active layers. 12,13,42 The fibers are hundreds of nanometers in length and are a result of p-DTS(FBTTh₂)₂ crystallization. ¹³ The hole mobility map (Figure 2b) features islands of moderate mobility (between 3 x 10⁻⁵ and 6 x 10⁻⁵ cm²/V·s) that are tens to hundreds of nanometers in size, with some islands containing mobility hot-spots (greater than 8 x 10⁻⁵ cm²/V·s).

A key factor that impacts charge transport in BHJs is the bicomponent nature of the films.^{9,10,37,38} The electron donating phase predominantly supports hole transport, while the electron accepting phase predominantly supports electron transport. As a result of

this, and the interpenetrating donor-acceptor structure of BHJs, holes (electrons) percolate through the donor (acceptor) phase of the film and are excluded from the acceptor (donor) phase. Charge transport is also impacted by nano- and mesoscale structural features, such as molecular orientation, 1,12,43,44 crystallinity, 25,37,45,46 and electrical continuity. In essence, charge percolation across a BHJ active layer depends on how much of a given phase is present (composition) and how efficiently the transport material is organized (connectivity).

In Figure 2, the regions of moderate and high mobility occasionally align with the elevated fibers, as might be anticipated given the expected donor-rich content of the fibers. Nevertheless, there is generally a lack of consistent correlation between hole mobility and topography (see Supporting Information Figure S2). As in earlier C-AFM studies, without further information about the internal structure or composition of the BHJ film, the main structural causes for local performance variations remain unclear.

To investigate the relationship between local hole mobility and donor concentration, we performed EF-TEM measurements at the same sample location as the PPIV hole mobility maps. An overview AFM topography scan was used as a reference to re-locate the sample area in the TEM. The process for obtaining donor concentration maps is outlined in Supporting Information Figure S3.

First, unfiltered and zero-loss TEM images were used to generate a relative thickness map, shown in Figure 2c. The relative thickness is given by $t \propto \ln(I_t/I_0)$, where I_t is the unfiltered signal, and I_0 is the zero-loss signal. The close correlation between the PPIV topography and TEM thickness confirms the successful retrieval of the same sample area and the consistency of the two measurement approaches. Slight differences between the two images can be attributed to AFM probe convolution while imaging high curvature features.

Next, EF-TEM was used to generate a sulfur elemental map with 2.7 nm pixel resolution (Supporting Information Figure S3). Since sulfur is present in p-DTS(FBTTh₂)₂ and not PC₇₁BM (Figure 1a), contrast in the elemental sulfur map corresponds to variations in the amount of donor material. To account for local differences in sample thickness, the sulfur map was divided by the thickness map to produce a donor concentration map (Figure 2d).⁴¹

It can be seen that the composition (Figure 2d) and thickness (Figure 2c) maps exhibit many similar features, supporting the expectation that the protruding fiber-like structures consist mainly of crystalline p-DTS(FBTTh₂)₂. Deviations between the composition and thickness maps can arise from overlapping distributions of less-ordered p-DTS(FBTTh₂)₂,

e.g., in finely intermixed domains, and from buried donor-rich or donor-depleted domains. A scatter plot of donor concentration versus AFM topography (shown in Supporting Information Figure S4) reveals a loosely correlated data set. The rough correlation between composition and topography justifies the use of topography as an approximate measure of relative local donor concentration for this BHJ system. Accurate analysis of local structure-function relationships, however, requires direct measurement of composition.

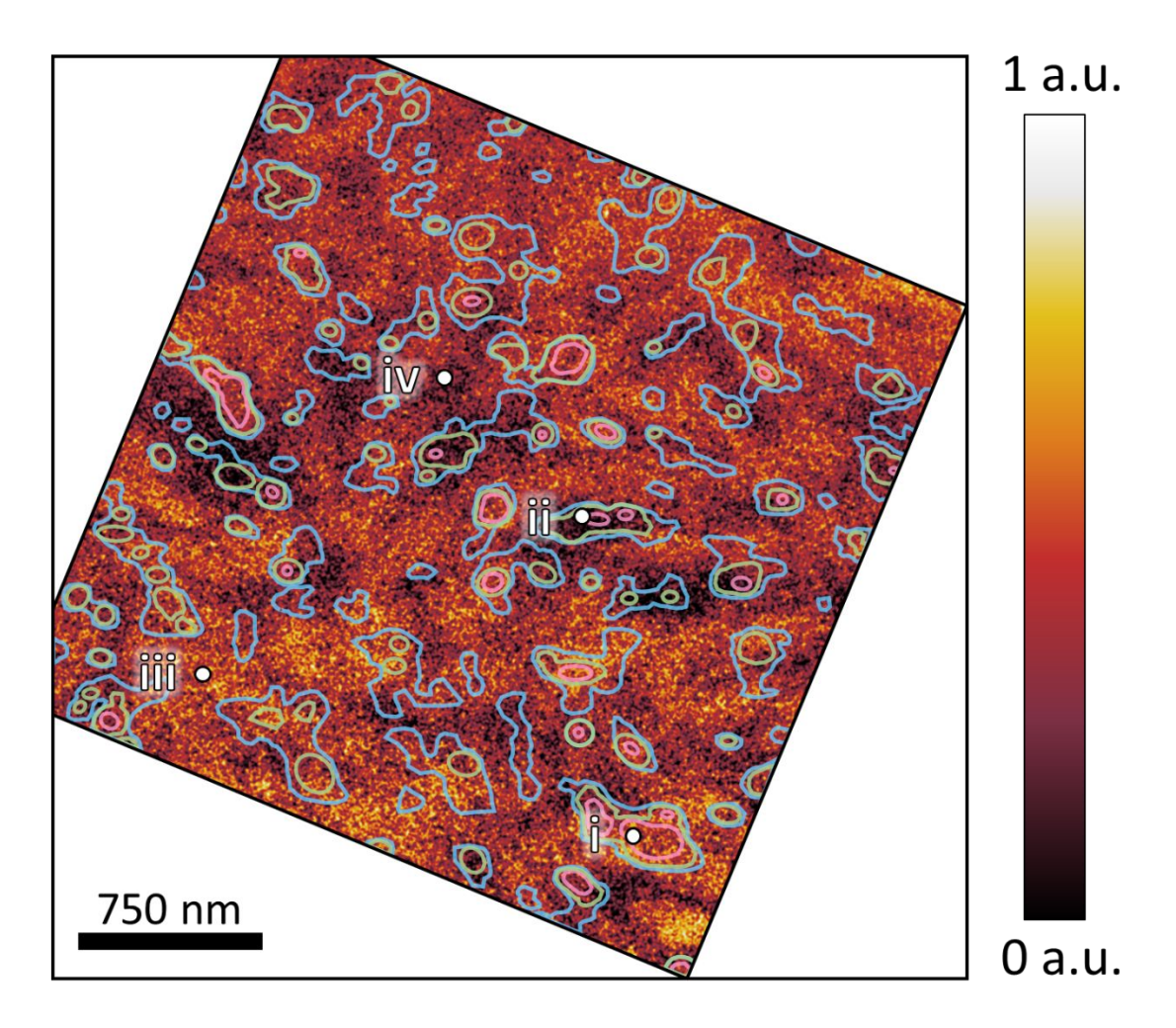


Figure 3. Donor concentration map with regions of high (>8 x 10^{-5} cm²/V·s), elevated (>6 x 10^{-5} cm²/V·s), and moderate (>3 x 10^{-5} cm²/V·s) hole mobility from Figure 2b outlined in red, green, and blue, respectively. The roman numerals identify locations that are discussed in the main text.

To analyze the links between hole mobility and donor concentration at the nanoscale, outlines of high, elevated, and moderate hole mobility regions (red, green, and blue,

respectively) were overlaid onto the donor concentration map (Figure 3). Surprisingly, there is little correlation between the local hole mobility and donor concentration. We document four types of behavior in Figure 3: at locations *i* and *iv*, hole mobility correlates with high and low levels of donor concentration. More common, however, are anticorrelated regions, such as locations *ii* and *iii*, where a high mobility region corresponds to low donor concentration and a low mobility region corresponds to high donor concentration. Other regions show islands of moderate and elevated hole mobility extending across a wide range of donor concentrations. A scatter plot of hole mobility versus composition (shown in the Supporting Information Figure S5) exhibits a broad distribution of mobility values for any given composition and no discernible trend. A second data set (Figure S6) from a different sample location also shows a lack of correlation between local hole mobility and donor concentration.

This behavior at the nanoscale is in contrast with device-scale measurements that show a clear, positive correlation between hole mobility and donor concentration in BHJ films. 9,25,53,54 These results also run counter to the common interpretation of EF-TEM and C-AFM data, that a high local donor concentration should imply a high hole mobility, and vice versa. It is interesting to note that, instead, regions such as location iii exhibit a low hole mobility, despite a high donor concentration. This shows that some donor-rich domains are poorly linked to transport pathways, perhaps due to a depletion of donor molecules in the surrounding intermixed areas during donor crystallization. Conversely, regions such as location ii exhibit a high hole mobility, despite a low local donor concentration, implying that finely intermixed regions, and not just pure domains, contribute substantially to charge percolation. It is remarkable that these regions with low donor content can outperform donor-rich sample locations. Despite the efficient hole transport expected in donor-rich domains, it is the intervening mixed regions that dictate whether holes ultimately flow across the BHJ. The observation that mixed domains play a decisive role in charge migration bolsters recent observations in other small molecule BHJs that show an absence of charge trapping and reduced nongeminate losses in active layers dominated by small, mixed domains.⁵⁵

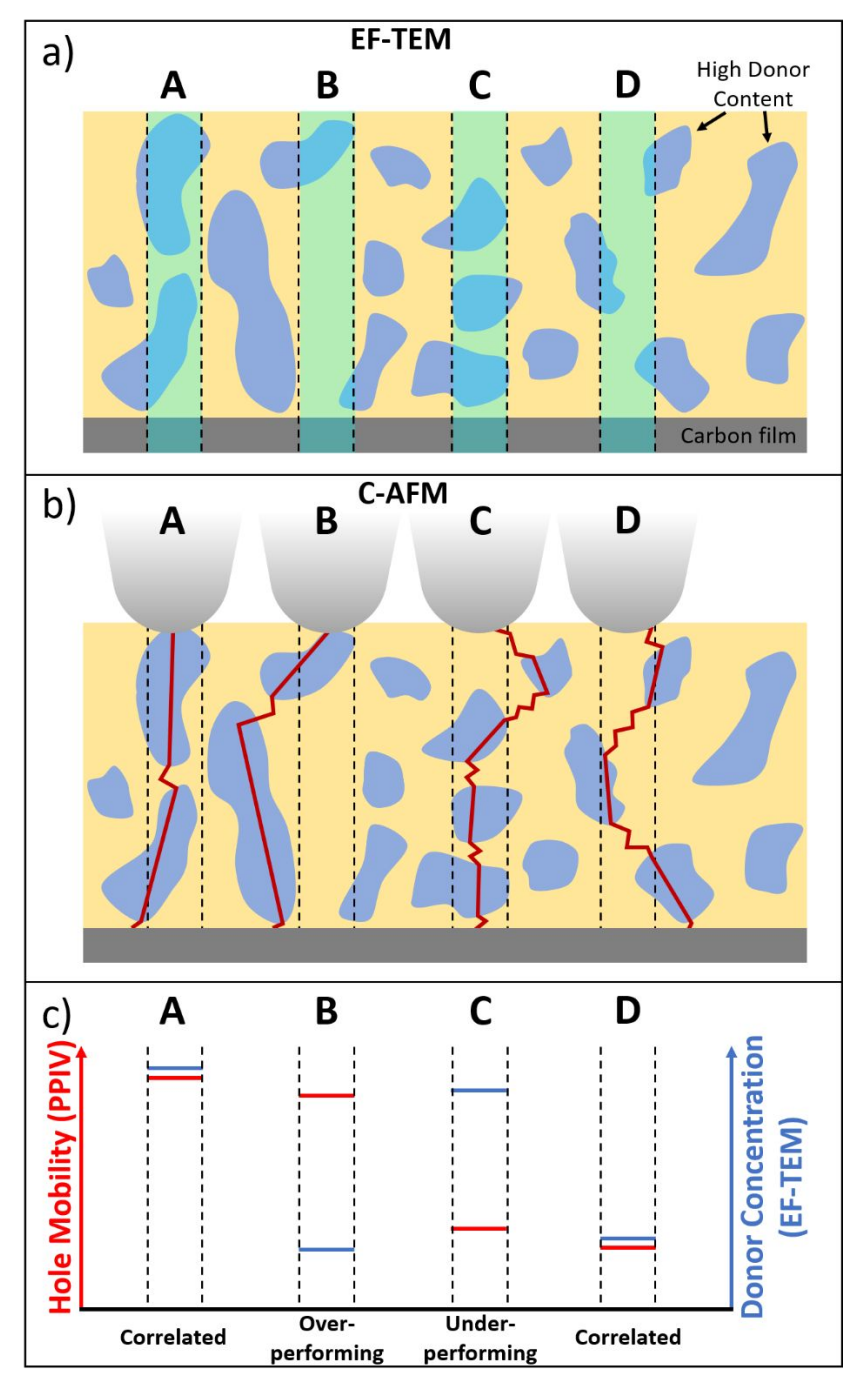


Figure 4. Illustrative examples of how local correlation or anticorrelation between donor concentration and hole mobility can occur. Donor-rich regions of the BHJ are represented in blue while donor-depleted regions are represented in yellow. (a) At a given measurement pixel, EF-TEM measures donor concentration within the underlying volume of the film (highlighted in light blue). (b) During PPIV mapping, current travels along preferred pathways (shown as red lines). (c) Donor concentration and hole mobility corresponding to the four cases represented in (a) and (b).

To understand the lack of correlation between the nanoscale hole mobility and donor concentration, we must also consider certain fundamental differences between EF-TEM and C-AFM measurements. EF-TEM composition maps present a two-dimensional projection of a three-dimensional interpenetrating network of donor and acceptor phases. Each pixel thus represents an average composition throughout a column of the sample (Figure 4a). C-AFM, on the other hand, measures current between a sharp (~25 nm radius) probe and a planar counter-electrode, leading to current spreading, with the current-carrying area broadening at lower sample depths. ^{36,56} Charge will also follow preferential pathways, i.e., paths of least resistance, as holes circumvent the electron acceptor phase and travel through well-connected donor regions (Figure 4b). As a result, charge percolates via three-dimensional pathways, with vertical and lateral components. ²⁵ Current recorded at the top surface of a BHJ active layer therefore shows where charge can be injected or extracted, but does not indicate the location of the buried conduction pathway(s) within the bulk of the film.

To illustrate how charge percolation is intertwined with local BHJ composition, we consider four scenarios in Figure 4. Cases A and B exhibit well-connected pathways, where charge mainly flows through domains with high donor concentration, leading to a high local hole mobility. In case A, the donor-rich charge transport pathway coincides with the column of data sampled by EF-TEM, leading to a correspondence between hole mobility and donor concentration. In case B, however, the preferential charge transport pathway mainly extends outside the EF-TEM sampling region for the given pixel location. This results in a low composition reading, despite the high local hole mobility. Such a region can be considered to be overperforming, since it yields a high hole mobility, even though the probed donor concentration is low. The cause of the overperformance in this case is the lateral access to a nearby donor-rich pathway. Other causes of overperformance can relate the efficiency of charge transport within the donor phase, e.g., due to high local crystallinity^{25,37,45,46,51,57} or favorable molecular orientation. 1,43,44,58

Cases C and D in Figure 4 show tortuous pathways for charge carriers, where charge navigates through donor-rich regions that are interspersed with donor-depleted regions. Within the donor-depleted regions, limited connectivity among the donor molecules leads to poor local hole mobility. In case C, the EF-TEM sampling region includes multiple donor-rich domains, resulting in a high composition reading. We consider such a region to be underperforming, since it yields a low hole mobility, despite the high local donor concentration. In case D, the donor-deficient transport pathway coincides with a column of low donor content sampled by EF-TEM, leading to a correspondence between hole mobility and donor concentration.

It should be noted that there are additional factors that can lead to anticorrelation between donor concentration and hole mobility. The relatively disordered structure in donor-depleted (mixed) regions will lead to variable connectivity between donor molecules. Therefore, the tortuosity of transport pathways is not only determined by the extent of the donor-rich or donor-depleted regions, rather it is sensitive to the local configuration of donor molecules along the pathways. For example, in case A of Figure 4, a discontinuity within the mixed region between donor-rich domains could lead to a low hole mobility. Alternatively, in case D, a high hole mobility could occur if the mixed regions along the transport pathway have a favorable arrangement of donor molecules.

From the above examples, it is apparent that local charge transport in a BHJ is intimately connected with local composition. The lack of correlation between hole mobility and donor concentration at the nanoscale, however, suggests that other structural traits mediate local charge transport, particularly in the over- and underperforming regions of the film. We attribute overperformance (underperformance) to the presence of well-connected (poorly-connected) donor pathways.

Electrical connectivity can be categorized into three types: continuity, crystallinity, and molecular orientation. Continuity depends on the presence of bottlenecks or breaks in the transporting phase. Crystallinity can also be thought of as a type of connectivity since well-ordered, close-packed molecules will have improved molecular orbital overlap that facilitates charge transport. Molecular orientation leads to connectivity along specific directions in which molecular orbital overlap is increased. Prof. 1,12,43,44 For instance, alkyl chains may impede transport along one direction, while π - π orbital overlap will enhance charge transport along another. π - π 0 orbital overlap will enhance

It should be noted that in the case of p-DTS(FBTTh₂)₂:PC₇₁BM active layers, the donor phase is predominantly edge-on with respect to the substrate, limiting the role of molecular orientation.²⁵ Nevertheless, since GIXD only characterizes crystalline portions of the film, there remains a possibility that mixed regions with limited molecular order contain face-on components.

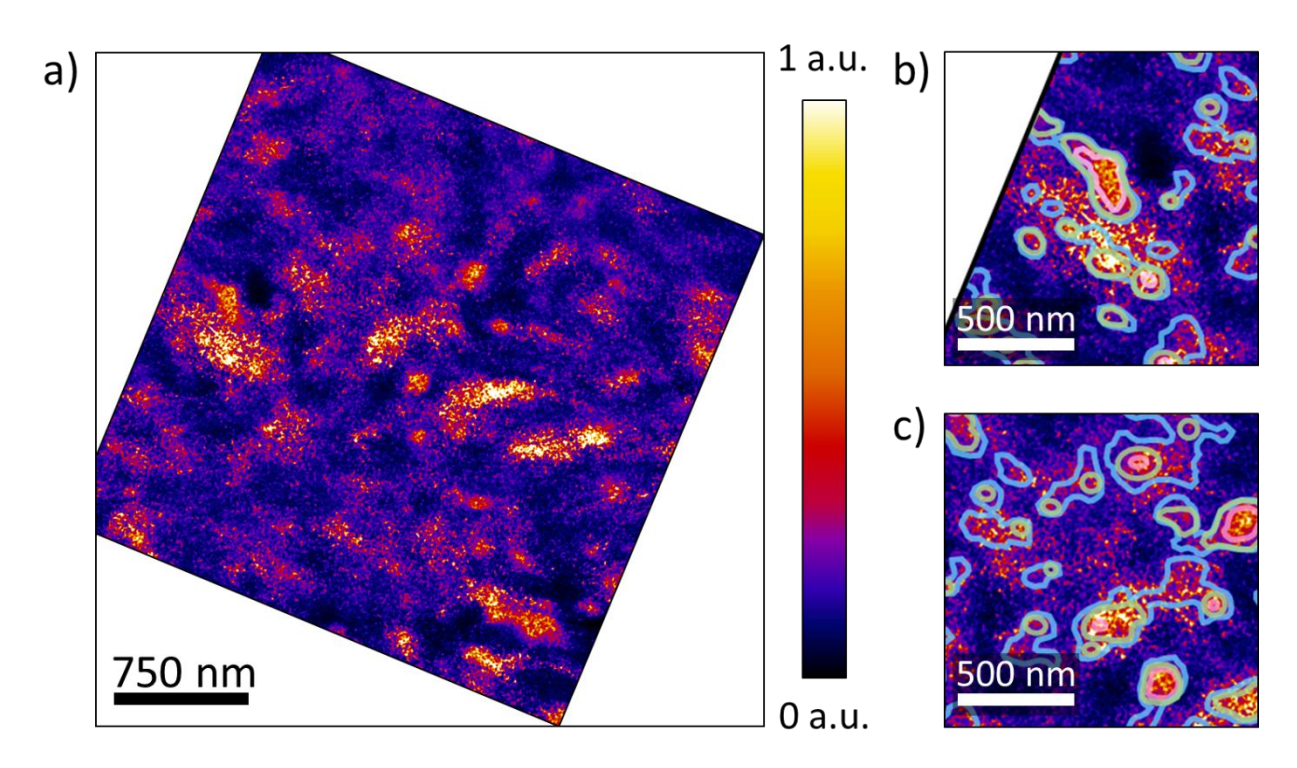


Figure 5. (a) Connectivity map generated by dividing hole mobility (Figure 2b) by donor concentration (Figure 2d). Bright regions represent areas that overperform (high mobility for the given donor concentration). (b,c) Selected regions showing the connectivity map overlaid with outlines of high (>8 x 10^{-5} cm²/V·s), elevated (>6 x 10^{-5} cm²/V·s), and moderate (>3 x 10^{-5} cm²/V·s) hole mobility.

To visualize regions of over- and under-performance due to local connectivity, we generated a "connectivity map" (Figure 5a) by dividing the normalized hole mobility map by the normalized donor concentration map. This analysis seeks to decouple the contribution of composition from other film properties that affect charge carrier mobility. The bright regions of the connectivity map represent overperforming areas (high hole mobility for a given donor concentration) that benefit from local crystallinity, favorable molecular orientation, or electrical continuity. On the other hand, the dark underperforming regions (low hole mobility for a given donor concentration) are negatively impacted by poor molecular order, unfavorable molecular orientation, or tortuous transport pathways.

Characteristic features of the connectivity map are presented in Figure 5b and 5c, which show selected regions overlaid with outlines representing the boundaries of high (red), elevated (green), and moderate (blue) hole mobility. The full connectivity map with overlaid mobility thresholds is shown in Supporting Information Figure S7. Figure 5b exhibits areas of high and elevated mobility that overlap regions of high connectivity,

which illustrates the most obvious relationship, that high connectivity can lead to high charge carrier mobility. Interestingly, many of the high connectivity regions correspond to regions with a low donor concentration, supporting the notion that finely mixed phases, rather than pure phases, play a dominant role in charge transport within small molecule BHJs.⁵⁵

It is also worth noting that some regions of high connectivity extend tens to hundreds of nanometers beyond the boundaries of the high and elevated hole mobility regions. This result suggests that the areas surrounding the high-performance regions overperform due to lateral access to the nearby mobility hot spots, which serve as preferred charge transport pathways. This observation is consistent with our recent study that identified the importance of lateral transport pathways during charge percolation across p-DTS(FBTTh₂)₂:PC₇₁BM active layers.²⁵

Other regions of intermediate and high connectivity are not neighboring high mobility locations, e.g. as seen at the center of Figure 5c, nearly 200 nm away from the closest high mobility region. The lack of proximity to nearby high mobility pathways indicates that these regions overperform as a result of intrinsic local connectivity, e.g., due to crystallinity, favorable molecular orientation, or electrical continuity. Connectivity maps can thus identify sample regions with structural configurations that enhance local electrical performance.

CONCLUSION

To evaluate the dependence of nanoscale charge transport on film composition in OPV active layers, we performed C-AFM PPIV hole mobility and EF-TEM composition mapping at the same location of a small molecule BHJ film. C-AFM provides insight into local electrical properties that is lacking in EF-TEM characterization, while EF-TEM provides compositional and structural information that can aid in interpreting local performance variations observed by C-AFM.

Surprisingly, these maps reveal that local hole mobility does not correlate with local composition, contrary to device-scale measurements that show a strong positive correlation between charge transport efficiency and transport material volume fraction. 9,25,53,54 Our results demonstrate that donor phase connectivity, rather than local donor amount, is the key feature that governs local hole transport across the BHJ. To decouple the contributions of donor concentration and connectivity, we generated a connectivity map to identify regions where local crystallinity, molecular orientation, and electrical continuity enhance charge transport.

The presented results hold implications for how EF-TEM and C-AFM data are interpreted for BHJ systems, as the results call into question the supposition that a high degree of local phase purity implies efficient local charge transport and vice versa. This work also supports an emerging picture for small molecule BHJs that implicates molecular order and continuity within finely mixed domains, and not domain purity, as the key requirement for efficient charge migration and collection.⁵⁵ Well-connected intermixed morphologies can be promoted through processing and supramolecular design strategies that suppress crystallization or enhance donor-acceptor miscibility.⁶¹

The devised colocalized TEM/AFM approach holds promise for elucidating nanoscale structure-function links in OPVs and other nanostructured systems. Future work can take advantage of the generalizable nature of the approach, to combine other AFM and TEM modes, such as photocurrent mapping or TEM tomography.

METHODS

Sample Preparation. Indium tin oxide (ITO) coated glass substrates (Colorado Concept Coatings LLC) were cleaned with acetone, isopropanol, and deionized water (5 minutes each) in an ultrasonic bath. After drying under nitrogen gas, the substrates were heated to 100 °C for 5 minutes and cleaned further using UV/ozone treatment. PEDOT:PSS (Clevios PH 1000 from Heraeus) was then spin-coated onto the substrates at 3000 RPM for 1 minute before drying on a hot plate at 150 °C for 20 minutes to yield a film thickness of approximately 30 nm. Carbon coated copper TEM grids (Ted Pella Inc.) were mounted on the PEDOT:PSS/ITO/glass substrates using small dabs of silver paint (Ted Pella Inc.) applied to the edge of the grid.

The active layer solution was prepared with a 3:2 weight ratio of $p\text{-DTS}(\text{FBTTh}_2)_2$ and PC₇₁BM, respectively (molecules supplied by Solaris Chem.) with a total concentration of 21 mg/ml in chlorobenzene (Sigma-Aldrich) and 0.8% v/v of solvent additive, 1,8-diiodooctane (Sigma-Aldrich). The solution was prepared and cast in a nitrogen-filled glovebox. Prior to spin-casting, the solution was stirred at 90 °C for 15 minutes and the substrate was placed on a 90 °C hot-plate for 5 min. Solutions were spin-coated onto the PEDOT:PSS/ITO/glass (with the carbon-coated TEM grids attached) after reaching 3000 RPM, to achieve a thickness of approximately 60 nm. After spin-casting, the samples were annealed at 75 °C for 15 min.

Conductive Atomic Force Microscopy. Nanoscale current and hole mobility measurements were performed in a nitrogen filled glovebox with an AIST-NT Combiscope AFM. Pt-coated AFM probes (BudgetSensors) were used with a spring constant of

0.2 N/m and tip radius of less than 25 nm. PPIV mapping involved recording current-voltage curves under a 7 nN applied force at 134,000 sample positions and extracting hole mobility using a modified space charged limited current analysis that accounts for the probe-sample geometry. The current-voltage curves were analyzed and converted to PPIV mobility maps using in-house-developed Mathematica code and Gwyddion software. The use of high work function electrodes ensured hole-only transport.

Transmission Electron Microscopy. Unfiltered, zero-loss, and sulfur elemental maps were recorded using a Thermo-Fisher Scientific Tecnai F20 TEM operating at 200 kV with a 10 pA beam current. The microscope was equipped with a monochromator and a Gatan Infina Spectrometer. The unfiltered image was acquired for one second and the zero-loss image was acquired for 1 second with a 20 eV window centered at 0 eV. Energy-loss images were acquired for 60 seconds with a slit width of 5 eV and a 5 eV step size. To generate an energy-loss background signal, a series of energy-loss images were acquired between 120 and 160 eV. The pre-edge background signal from the energy-loss windows was fit to an exponential function and extrapolated to 200 eV. Sulfur elemental maps were generated by integrating the background-subtracted energy-loss signal over a range of 165 eV (the core-loss excitation edge for sulfur) to 200 eV.

Image Processing. Image processing and calculations were performed with Gwyddion and ImageJ software utilizing the Cornell Spectrum Imager plugin. $^{62-64}$ Zero-loss and unfiltered TEM images were used to extract relative thickness maps. The thickness and sulfur maps were flipped, rotated, and cropped to align with the AFM topography. Image alignment was achieved by comparing the AFM topography map with the TEM thickness map. The AFM maps were slightly stretched (by 0.5%) along the slow-scan direction to correct for sample drift and match the TEM images. The sulfur map was then divided by the thickness map to obtain a sulfur (p-DTS(FBTTh₂)₂) composition map. To generate the connectivity map, the hole mobility map was normalized and bicubically interpolated to the same pixel resolution as the TEM images and then divided by a normalized composition map. A flow chart outlining the image processing steps can be found in the Supporting Information (Figure S3).

ACKNOWLEDGEMENTS

This work was supported by the National Science Foundation (CAREER award DMR-1555028) and made use of the Cornell Center for Materials Research Shared Facilities, which are supported through the NSF MRSEC program (DMR-1719875). The authors thank Megan Holtz and Berit Goodge for assistance with TEM measurements and analysis.

ASSOCIATED CONTENT

Supporting Information available: C-AFM topography and current maps; hole mobility overlaid onto topography; image processing flow chart; height versus composition scatter plot; composition versus hole mobility scatter plot; hole mobility overlaid onto connectivity

References

- (1) Chen, W.; Qi, D. C.; Huang, H.; Gao, X.; Wee, A. T. S. Organic-Organic Heterojunction Interfaces: Effect of Molecular Orientation. *Adv. Funct. Mater.* **2011**, *21*, 410–424.
- (2) Darling, S. B.; You, F. The Case for Organic Photovoltaics. *RSC Adv.* **2013**, *3*, 17633–17648.
- (3) Huang, Y.; Kramer, E. J.; Heeger, A. J.; Bazan, G. C. Bulk Heterojunction Solar Cells: Morphology and Performance Relationships. *Chem. Rev.* **2014**, *114*, 7006–7043.
- (4) Meredith, P.; Armin, A. Scaling of next Generation Solution Processed Organic and Perovskite Solar Cells. *Nat. Commun.* **2018**, *9*, 5261.
- (5) Meng, L.; Zhang, Y.; Wan, X.; Li, C.; Zhang, X.; Wang, Y.; Ke, X.; Xiao, Z.; Ding, L.; Xia, R.; Yip, H.; Cao, Y.; Chen, Y. Organic and Solution-Processed Tandem Solar Cells with 17.3% Efficiency. *Science* 2018, 2612, 1094–1098.
- (6) Bartesaghi, D.; Pérez, I. del C.; Kniepert, J.; Roland, S.; Turbiez, M.; Neher, D.; Koster, L. J. A. Competition between Recombination and Extraction of Free Charges Determines the Fill Factor of Organic Solar Cells. *Nat. Commun.* **2015**, 6, 7083.
- (7) Yoshikawa, S.; Saeki, A.; Saito, M.; Osaka, I.; Seki, S. On the Role of Local Charge Carrier Mobility in the Charge Separation Mechanism of Organic Photovoltaics. *Phys. Chem. Chem. Phys.* **2015**, *17*, 17778–17784.
- (8) Collins, S. D.; Ran, N. A.; Heiber, M. C.; Nguyen, T. Q. Small Is Powerful: Recent Progress in Solution-Processed Small Molecule Solar Cells. *Adv. Energy Mater.* **2017**, *7*, 1602242.
- (9) Vakhshouri, K.; Kozub, D. R.; Wang, C.; Salleo, A.; Gomez, E. D. Effect of Miscibility and Percolation on Electron Transport in Amorphous Poly(3-Hexylthiophene)/Phenyl-C 61-Butyric Acid Methyl Ester Blends. *Phys. Rev. Lett.* **2012**, *108*, 026601.
- (10) Love, J. A.; Nagao, I.; Huang, Y.; Kuik, M.; Gupta, V.; Takacs, C. J.; Coughlin, J. E.; Qi, L.; Van Der Poll, T. S.; Kramer, E. J.; Heeger, A. J.; Nguyen, T.-Q.; Bazan, G. C. Silaindacenodithiophene-Based Molecular Donor: Morphological Features and Use in the Fabrication of Compositionally Tolerant, High-Efficiency Bulk Heterojunction Solar Cells. J. Am. Chem. Soc. 2014, 136, 3597–3606.
- (11) Perez, L. A.; Rogers, J. T.; Brady, M. A.; Sun, Y.; Welch, G. C.; Schmidt, K.; Toney, M. F.; Jinnai, H.; Heeger, A. J.; Chabinyc, M. L.; Bazan, G. C.; Kramer, E. J. The Role of Solvent Additive Processing in High Performance Small Molecule Solar Cells. *Chem. Mater.* **2014**, *26*, 6531–6541.
- (12) Takacs, C. J.; Collins, S. D.; Love, J. A.; Mikhailovsky, A. A.; Wynands, D.; Bazan, G. C.; Nguyen, T.-Q.; Heeger, A. J. Mapping Orientational Order in a Bulk

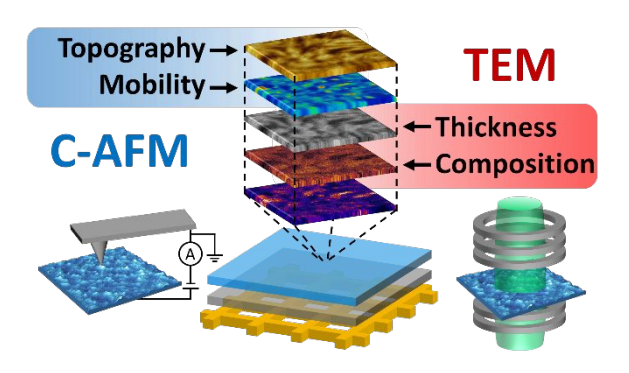
- Heterojunction Solar Cell with Polarization-Dependent Photoconductive Atomic Force Microscopy. *ACS Nano* **2014**, *8*, 8141–8151.
- (13) Love, J. A.; Proctor, C. M.; Liu, J.; Takacs, C. J.; Sharenko, A.; Van Der Poll, T. S.; Heeger, A. J.; Bazan, G. C.; Nguyen, T.-Q. Film Morphology of High Efficiency Solution-Processed Small-Molecule Solar Cells. *Adv. Funct. Mater.* **2013**, *23*, 5019–5026.
- (14) Ran, N. A.; Roland, S.; Love, J. A.; Savikhin, V.; Takacs, C. J.; Fu, Y. T.; Li, H.; Coropceanu, V.; Liu, X.; Brédas, J. L.; Bazan, G. C.; Toney, M. F.; Neher, Di.; Nguyen, T. Q. Impact of Interfacial Molecular Orientation on Radiative Recombination and Charge Generation Efficiency. *Nat. Commun.* **2017**, *8*, 79.
- (15) Takacs, C. J.; Sun, Y.; Welch, G. C.; Perez, L. a; Liu, X.; Wen, W.; Bazan, G. C.; Heeger, A. J. Solar Cell Efficiency, Self-Assembly, and Dipole-Dipole Interactions of Isomorphic Narrow-Band-Gap Molecules. *J. Am. Chem. Soc.* **2012**, *134*, 16597–16606.
- (16) Pfannmöller, M.; Flügge, H.; Benner, G.; Wacker, I.; Sommer, C.; Hanselmann, M.; Schmale, S.; Schmidt, H.; Hamprecht, F. A.; Rabe, T.; Kowalsky, W.; Schröder, R. R. Visualizing a Homogeneous Blend in Bulk Heterojunction Polymer Solar Cells by Analytical Electron Microscopy. *Nano Lett.* **2011**, *11*, 3099–3107.
- (17) van Bavel, S.; Sourty, E.; de With, G.; Veenstra, S.; Loos, J. Three-Dimensional Nanoscale Organization of Polymer Solar Cells. *J. Mater. Chem.* **2009**, *19*, 5388–5393.
- (18) Kozub, D. R.; Vakhshouri, K.; Orme, L. M.; Wang, C.; Hexemer, A.; Gomez, E. D. Polymer Crystallization of Partially Miscible Polythiophene/Fullerene Mixtures Controls Morphology. *Macromolecules* **2011**, *44*, 5722–5726.
- (19) Foster, S.; Deledalle, F.; Mitani, A.; Kimura, T.; Kim, K. B.; Okachi, T.; Kirchartz, T.; Oguma, J.; Miyake, K.; Durrant, J. R.; Doi, S.; Nelson, J. Electron Collection as a Limit to Polymer:PCBM Solar Cell Efficiency: Effect of Blend Microstructure on Carrier Mobility and Device Performance in PTB7:PCBM. Adv. Energy Mater. 2014, 4, 1400311.
- (20) Hammond, M. R.; Kline, R. J.; Herzing, A. A.; Richter, L. J.; Germack, D. S.; Ro, H. W.; Soles, C. L.; Fischer, D. A.; Xu, T.; Yu, L.; Toney, M. F.; Delongchamp, D. M. Molecular Order in High-Efficiency Polymer/Fullerene Bulk Heterojunction Solar Cells. ACS Nano 2011, 5, 8248–8257.
- (21) Mativetsky, J. M.; Loo, Y.-L.; Samorì, P. Elucidating the Nanoscale Origins of Organic Electronic Function by Conductive Atomic Force Microscopy. *J. Mater. Chem. C* **2014**, *2*, 3118–3128.
- (22) Musumeci, C.; Liscio, A.; Palermo, V.; Samorì, P. Electronic Characterization of Supramolecular Materials at the Nanoscale by Conductive Atomic Force and Kelvin Probe Force Microscopies. *Mater. Today* 2014, 17, 504–517.
- (23) Osaka, M.; Benten, H.; Ohkita, H.; Ito, S.; Ogawa, H.; Kanaya, T. Nanostructures for Efficient Hole Transport in Poly(3-Hexylthiophene) Film: A Study by Conductive Atomic Force Microscopy. *J. Phys. Chem. C* **2015**, *119*, 24307–24314.
- (24) Osaka, M.; Benten, H.; Ohkita, H.; Ito, S. Intermixed Donor/Acceptor Region in Conjugated Polymer Blends Visualized by Conductive Atomic Force Microscopy.

- Macromolecules 2017, 50, 1618-1625.
- (25) Mehta, J. S.; Mativetsky, J. M. In-Plane Pathways Facilitate out-of-Plane Charge Transport in Organic Solar Cell Active Layers. *ACS Appl. Energy Mater.* **2018**, *1*, 5656–5662.
- (26) Dante, M.; Peet, J.; Nguyen, T. Q. Nanoscale Charge Transport and Internal Structure of Bulk Heterojunction Conjugated Polymer/Fullerene Solar Cells by Scanning Probe Microscopy. *J. Phys. Chem. C* **2008**, *112*, 7241–7249.
- (27) Osaka, M.; Benten, H.; Lee, L. T.; Ohkita, H.; Ito, S. Development of Highly Conductive Nanodomains in Poly(3-Hexylthiophene) Films Studied by Conductive Atomic Force Microscopy. *Polym. (United Kingdom)* **2013**, *54*, 3443–3447.
- (28) Groves, C.; Reid, O. G.; Ginger, D. S. Heterogeneity in Polymer Solar Cells: Local Morphology and Performance in Organic Photovoltaics Studied with Scanning Probe Microscopy. *Acc. Chem. Res.* **2010**, *43*, 612–620.
- (29) Coffey, D. C.; Reid, O. G.; Rodovsky, D. B.; Bartholomew, G. P.; Ginger, D. S. Mapping Local Photocurrents in Polymer/Fullerene Solar Cells with Photoconductive Atomic Force Microscopy. *Nano Lett.* 2007, 7, 738–744.
- (30) Vakhshouri, K.; Kesava, S. V.; Kozub, D. R.; Gomez, E. D. Characterization of the Mesoscopic Structure in the Photoactive Layer of Organic Solar Cells: A Focused Review. *Mater. Lett.* **2013**, *90*, 97–102.
- (31) Hoven, C. V.; Dang, X.-D.; Coffin, R. C.; Peet, J.; Nguyen, T.-Q.; Bazan, G. C. Improved Performance of Polymer Bulk Heterojunction Solar Cells Through the Reduction of Phase Separation via Solvent Additives. *Adv. Mater.* **2010**, *22*, E63–E66.
- (32) Rice, A. H.; Giridharagopal, R.; Zheng, S. X.; Ohuchi, F. S.; Ginger, D. S.; Luscombe, C. K. Controlling Vertical Morphology within the Active Layer of Organic Photovoltaics Using Poly(3-Hexylthiophene) Nanowires and Phenyl-C 61-Butyric Acid Methyl Ester. *ACS Nano* **2011**, *5*, 3132–3140.
- (33) Pingree, L. S. C.; Reid, O. G.; Ginger, D. S. Imaging the Evolution of Nanoscale Photocurrent Collection Networks During Annealing of Polythiphene/Fullerene Solar Cells. *Nano Lett.* **2009**, *9*, 2946–2952.
- (34) Button, S. W.; Mativetsky, J. M. High-Resolution Charge Carrier Mobility Mapping of Heterogeneous Organic Semiconductors. *Appl. Phys. Lett.* **2017**, *111*, 083302.
- (35) Qiu, H.; Shim, J. H.; Cho, J. Nanoscale Insight into Performance Loss Mechanisms in P3HT:ZnO Nanorod Solar Cells. *ACS Appl. Energy Mater.* **2018**, *1*, 6172–6180.
- (36) Reid, O. G.; Munechika, K.; Ginger, D. S. Space Charge Limited Current Measurements on Conjugated Polymer Films Using Conductive Atomic Force Microscopy. *Nano Lett.* **2008**, *8*, 1602–1609.
- (37) Mukherjee, S.; Proctor, C. M.; Tumbleston, J. R.; Bazan, G. C.; Nguyen, T.-Q.; Ade, H. Importance of Domain Purity and Molecular Packing in Efficient Solution-Processed Small-Molecule Solar Cells. *Adv. Mater.* **2015**, *27*, 1105–1111.
- (38) Levon, K.; Margolina, A.; Patashinsky, A. Z. Multiple Percolation in Conducting Polymer Blends. *Macromolecules* **1993**, *26*, 4061–4063.
- (39) Kyaw, A. K. K.; Wang, D. H.; Wynands, D.; Zhang, J.; Nguyen, T.-Q.; Bazan, G. C.; Heeger, A. J. Improved Light Harvesting and Improved Efficiency by Insertion of an Optical Spacer (ZnO) in Solution-Processed Small-Molecule Solar Cells.

- Nano Lett. **2013**, 13, 3796–3801.
- (40) Herzing, A. A.; Richter, L. J.; Anderson, I. M. 3D Nanoscale Characterization of Thin-Film Organic Photovoltaic Device Structures via Spectroscopic Contrast in the TEM. J. Phys. Chem. C 2010, 114, 17501–17508.
- (41) Kuei, B.; Kabius, B.; Gray, J. L.; Gomez, E. D. Strategies for Elemental Mapping from Energy-Filtered TEM of Polymeric Materials. *MRS Commun.* **2018**, *8*, 1321–1327.
- (42) Engmann, S.; Bokel, F. A.; Herzing, A. A.; Ro, H. W.; Girotto, C.; Caputo, B.; Hoven, C. V.; Schaible, E.; Hexemer, A.; DeLongchamp, D. M.; Richter, L. J. Real-Time X-Ray Scattering Studies of Film Evolution in High Performing Small-Molecule—Fullerene Organic Solar Cells. J. Mater. Chem. A 2015, 3, 8764–8771.
- (43) Verploegen, E.; Mondal, R.; Bettinger, C. J.; Sok, S.; Toney, M. F.; Bao, Z. Effects of Thermal Annealing upon the Morphology of Polymer-Fullerene Blends. *Adv. Funct. Mater.* **2010**, *20*, 3519–3529.
- (44) Bai, X.; Zong, K.; Ly, J.; Mehta, J. S.; Hand, M.; Molnar, K.; Lee, S.; Kahr, B.; Mativetsky, J. M.; Briseno, A.; Lee, S. S. Orientation Control of Solution-Processed Organic Semiconductor Crystals To Improve Out-of-Plane Charge Mobility. Chem. Mater. 2017, 29, 7571–7578.
- (45) Sharenko, A.; Kuik, M.; Toney, M. F.; Nguyen, T.-Q. Crystallization-Induced Phase Separation in Solution-Processed Small Molecule Bulk Heterojunction Organic Solar Cells. *Adv. Funct. Mater.* **2014**, *24*, 3543–3550.
- (46) Kyaw, A. K. K.; Wang, D. H.; Luo, C.; Cao, Y.; Nguyen, T.-Q.; Bazan, G. C.; Heeger, A. J. Effects of Solvent Additives on Morphology, Charge Generation, Transport, and Recombination in Solution-Processed Small-Molecule Solar Cells. *Adv. Energy Mater.* **2014**, *4*, 1301469.
- (47) Kirkpatrick, S. Percolation and Conduction. Rev. Mod. Phys. 1973, 45, 574–588.
- (48) Wodo, O.; Roehling, J. D.; Moulé, A. J.; Ganapathysubramanian, B. Quantifying Organic Solar Cell Morphology: A Computational Study of Three-Dimensional Maps. *Energy Environ. Sci.* 2013, 6, 3060–3070.
- (49) Noriega, R.; Rivnay, J.; Vandewal, K.; Koch, F. P. V; Stingelin, N.; Smith, P.; Toney, M. F.; Salleo, A. A General Relationship between Disorder, Aggregation and Charge Transport in Conjugated Polymers. *Nat. Mater.* **2013**, *12*, 1038–1044.
- (50) Roehling, J. D.; Batenburg, K. J.; Swain, F. B.; Moulé, A. J.; Arslan, I. Three-Dimensional Concentration Mapping of Organic Blends. *Adv. Funct. Mater.* **2013**, 23, 2115–2122.
- (51) Giridharagopal, R.; Ginger, D. S. Characterizing Morphology in Bulk Heterojunction Organic Photovoltaic Systems. *J. Phys. Chem. Lett.* **2010**, *1*, 1160–1169.
- (52) Leapman, R. D.; Fiori, C. E.; Swyt, C. R. Mass Thickness Determination by Electron Energy Loss for Quantitative X-ray Microanalysis in Biology. *J. Microsc.* **1984**, *133*, 239–253.
- (53) Pranculis, V.; Ruseckas, A.; Vithanage, D. A.; Hedley, G. J.; Samuel, I. D. W.; Gulbinas, V. Influence of Blend Ratio and Processing Additive on Free Carrier Yield and Mobility in PTB7:PC71bm Photovoltaic Solar Cells. *J. Phys. Chem. C* **2016**, *120*, 9588–9594.
- (54) Proctor, C. M.; Kher, A. S.; Love, J. A.; Huang, Y.; Sharenko, A.; Bazan, G. C.;

- Nguyen, T.-Q. Understanding Charge Transport in Molecular Blend Films in Terms of Structural Order and Connectivity of Conductive Pathways. *Adv. Energy Mater.* **2016**, *6*, 1502285.
- (55) Alqahtani, O.; Babics, M.; Gorenflot, J.; Savikhin, V.; Ferron, T.; Balawi, A. H.; Paulke, A.; Kan, Z.; Pope, M.; Clulow, A. J.; Wolf, J.; Burn, P. L.; Gentle, I. R.; Neher, D.; Toney, M. F.; Laquai, F.; Beaujuge, P. M.; Collins, B. A. Mixed Domains Enhance Charge Generation and Extraction in Bulk-Heterojunction Solar Cells with Small-Molecule Donors. *Adv. Energy Mater.* **2018**, *8*, 1702941.
- (56) Qiu, H.; Dong, X.; Shim, J. H.; Cho, J.; Mativetsky, J. M. Effective Charge Collection Area during Conductive and Photoconductive Atomic Force Microscopy. Appl. Phys. Lett. 2018, 112, 263102.
- (57) Mativetsky, J. M.; Wang, H.; Lee, S. S.; Whittaker-Brooks, L.; Loo, Y.-L. Face-on Stacking and Enhanced out-of-Plane Hole Mobility in Graphene-Templated Copper Phthalocyanine. *Chem. Commun.* **2014**, *50*, 5319–5321.
- (58) O'Connor, B.; Kline, R. J.; Conrad, B. R.; Richter, L. J.; Gundlach, D.; Toney, M. F.; DeLongchamp, D. M. Anisotropic Structure and Charge Transport in Highly Strain-Aligned Regioregular Poly(3-Hexylthiophene). *Adv. Funct. Mater.* **2011**, *21*, 3697–3705.
- (59) Mukherjee, S.; Proctor, C. M.; Bazan, G. C.; Nguyen, T.-Q.; Ade, H. Significance of Average Domain Purity and Mixed Domains on the Photovoltaic Performance of High-Efficiency Solution-Processed Small-Molecule BHJ Solar Cells. Adv. Energy Mater. 2015, 5, 1500877.
- (60) Coropceanu, V.; Cornil, J.; da Silva Filho, D. A.; Olivier, Y.; Silbey, R.; Bredas, J.-L. Charge Transport in Organic Semiconductors. *Chem. Rev.* 2007, 107, 926–952.
- (61) Haruk, A. M.; Mativetsky, J. M. Supramolecular Approaches to Nanoscale Morphological Control in Organic Solar Cells. *Int. J. Mol. Sci.* **2015**, *16*, 13381–13406.
- (62) Nečas, D.; Klapetek, P. Gwyddion: An Open-Source Software for SPM Data Analysis. *Cent. Eur. J. Phys.* **2012**, *10*, 181–188.
- (63) Schneider, C. A.; Rasband, W. S.; Eliceiri, K. W. NIH Image to ImageJ: 25 Years of Image Analysis. *Nat. Methods* **2012**, *9*, 671–675.
- (64) Hovden, R.; Cueva, P.; Mundy, J. A.; Muller, D. A. The Open-Source Cornell Spectrum Imager. *Micros. Today* **2012**, *21*, 40–44.

Table of contents graphic:



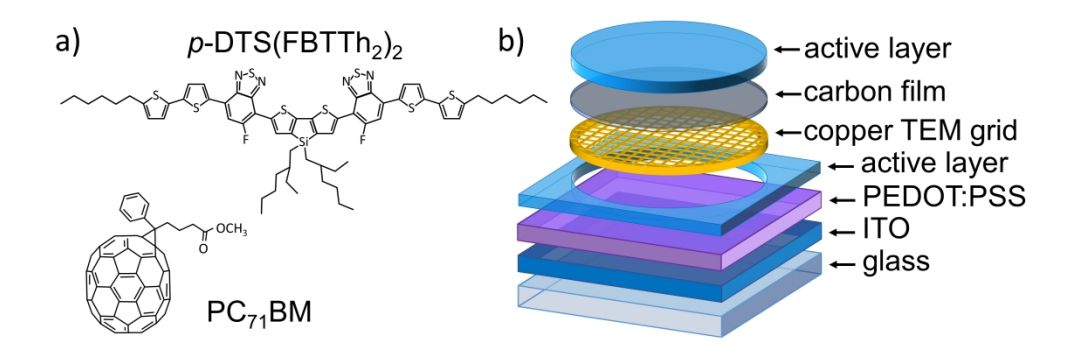


Figure 1. (a) Molecular structure of p-DTS(FBTTh2)2 and PC71BM. (b) Exploded view of the sample structure.

290x104mm (300 x 300 DPI)

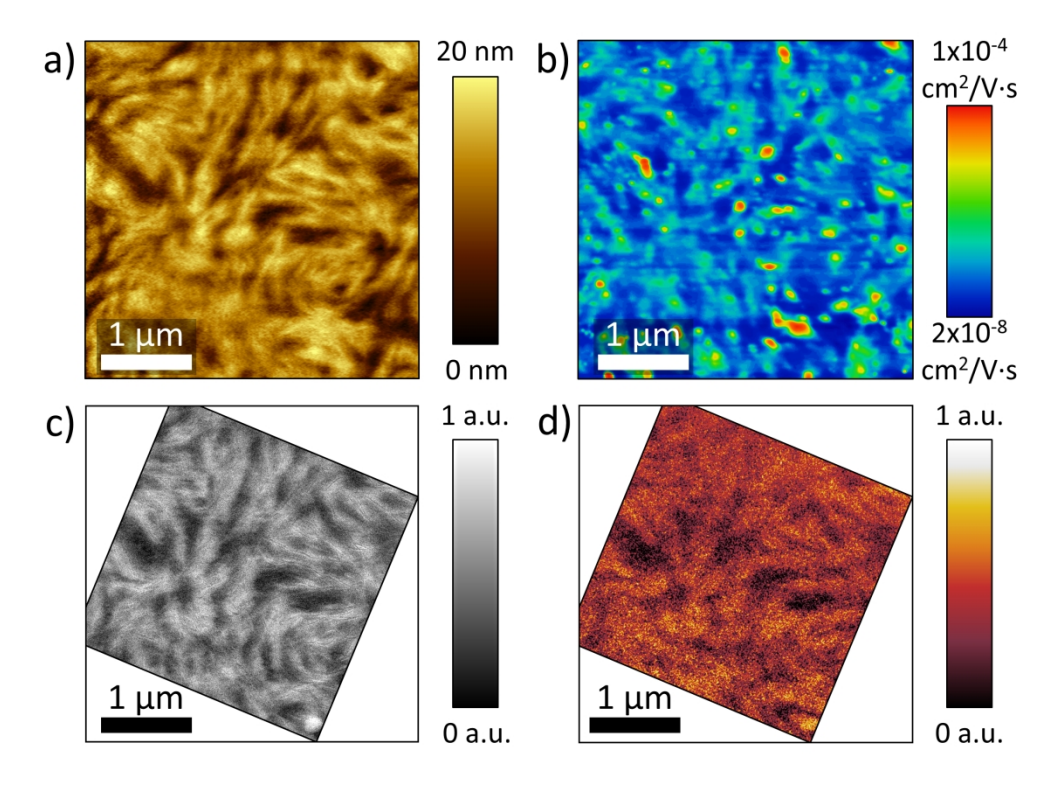


Figure 2. Structural and electrical mapping at the same location of a p DTS(FBTTh2)2:PC71BM film: (a) topography acquired during PPIV mapping, (b) PPIV hole mobility, (c) thickness measured by TEM, and (d) donor concentration.

228x167mm (300 x 300 DPI)

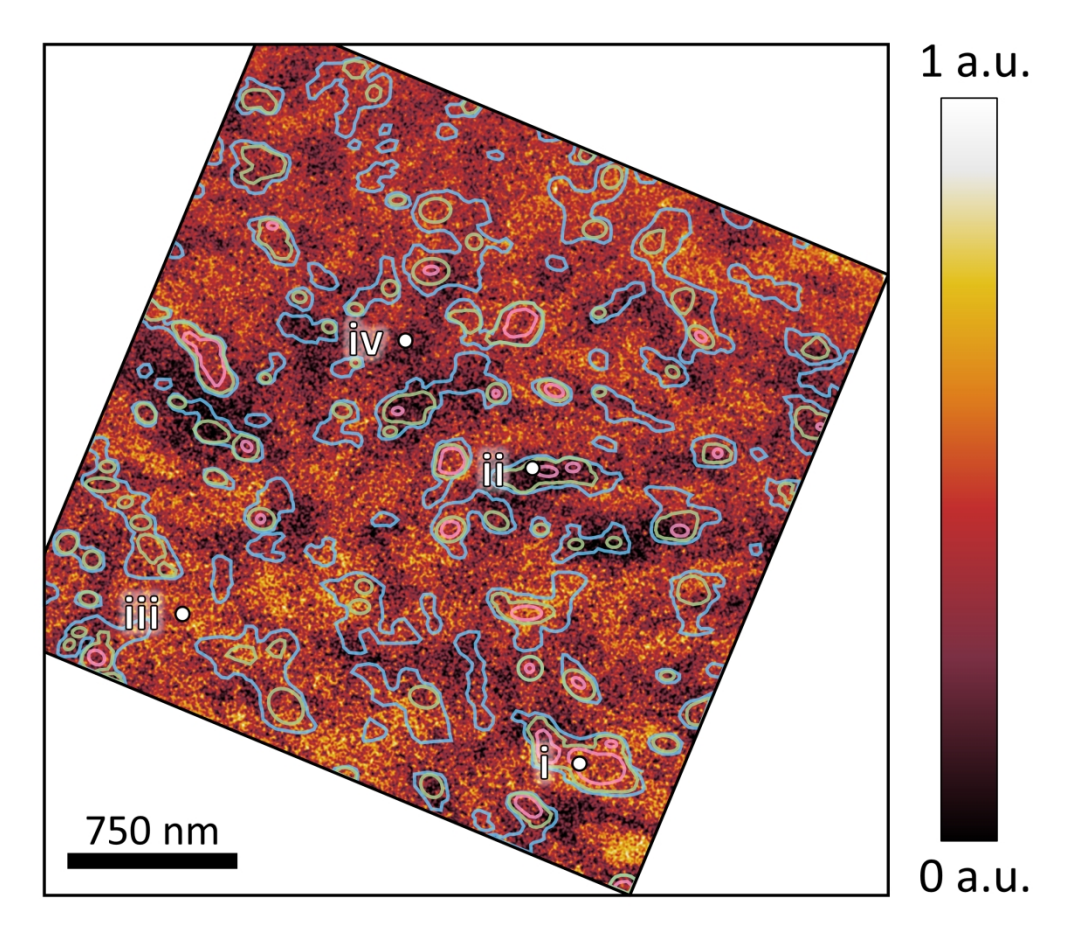


Figure 3. Donor concentration map with regions of high ($>8 \times 10$ -5 cm2/V·s), elevated ($>6 \times 10$ -5 cm2/V·s), and moderate ($>3 \times 10$ -5 cm2/V·s) hole mobility from Figure 2b outlined in red, green, and blue, respectively. The roman numerals identify locations that are discussed in the main text.

224x198mm (300 x 300 DPI)

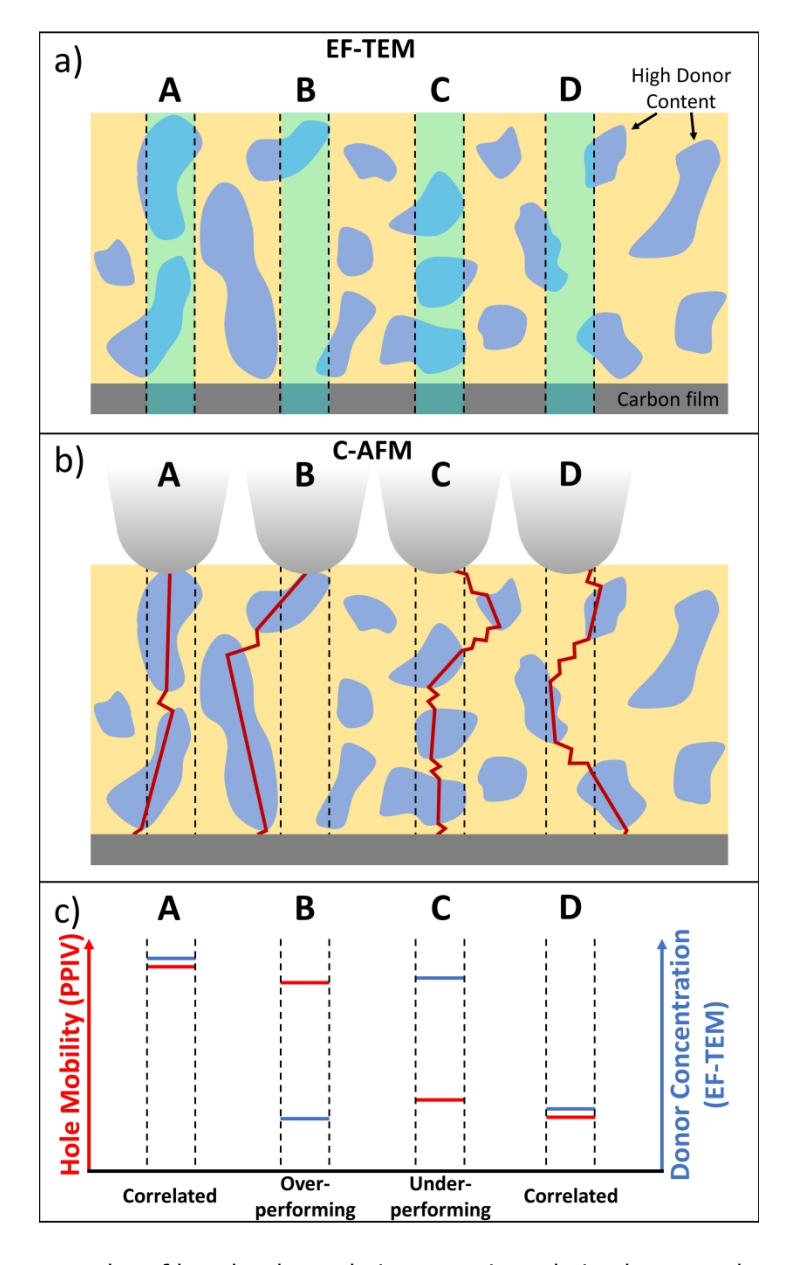


Figure 4. Illustrative examples of how local correlation or anticorrelation between donor concentration and hole mobility can occur. Donor-rich regions of the BHJ are represented in blue while donor-depleted regions are represented in yellow. (a) At a given measurement pixel, EF-TEM measures donor concentration within the underlying volume of the film (highlighted in light blue). (b) During PPIV mapping, current travels along preferred pathways (shown as red lines). (c) Donor concentration and hole mobility corresponding to the four cases represented in (a) and (b).

211x351mm (300 x 300 DPI)

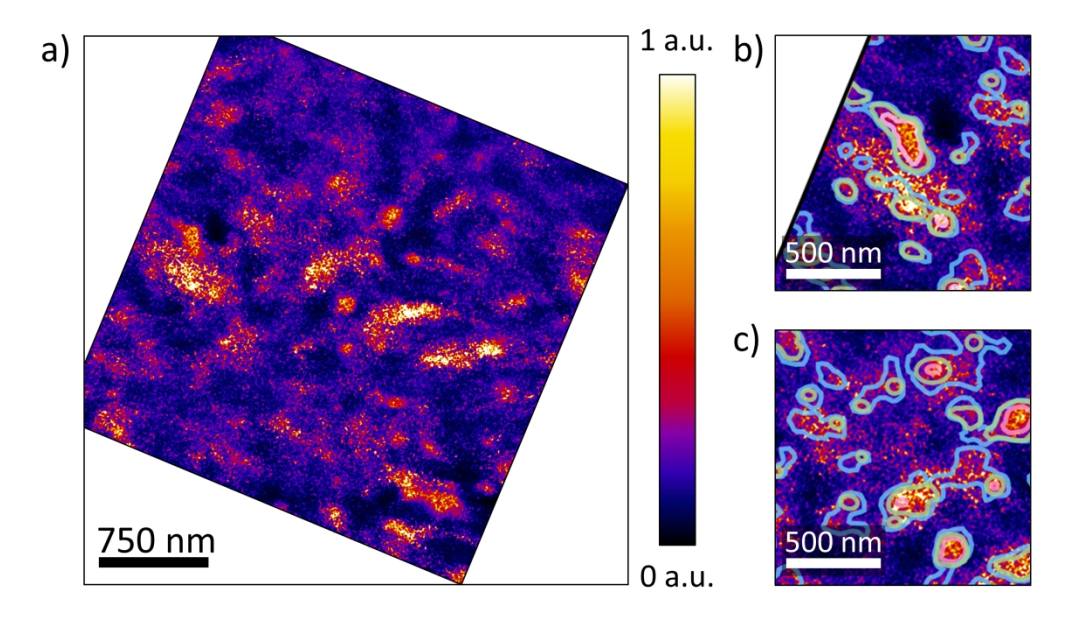


Figure 5. (a) Connectivity map generated by dividing hole mobility (Figure 2b) by donor concentration (Figure 2d). Bright regions represent areas that overperform (high mobility for the given donor concentration). (b,c) Selected regions showing the connectivity map overlaid with outlines of high ($>8 \times 10-5 \text{ cm}/\text{V·s}$), elevated ($>6 \times 10-5 \text{ cm}/\text{V·s}$), and moderate ($>3 \times 10-5 \text{ cm}/\text{V·s}$) hole mobility.

253x147mm (300 x 300 DPI)

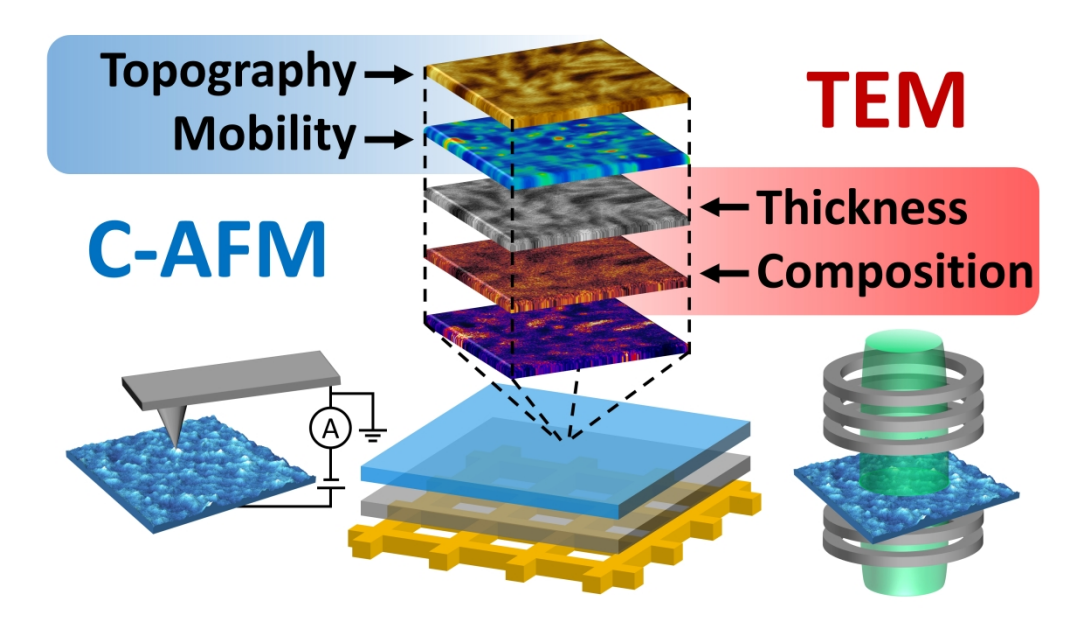


Table of contents graphic 320x187mm (300 x 300 DPI)